Multi-Physical Domain Modeling of a DFIG Wind Turbine System using PLECS®

Min Luo
Plexim GmbH
Technoparkstrasse 1
8005 Zürich Switzerland

1 Introduction

A cost and energy efficient method of wind power generation is to connect the output of the turbine to a doubly-fed induction generator (DFIG), allowing operation at a range of variable speeds. While for electrical engineers the electromagnetic components in such a system, like the electric machine, power electronic converter and magnetic filters are of most interest, a DFIG wind turbine is a complex design involving multiple physical domains strongly interacting with each other. The electrical system, for instance, is influenced by the converter's cooling system and mechanical components, including the rotor blades, shaft and gearbox. This means that during component selection and design of control schemes, the influence of domains on one another must be considered in order to achieve an optimized overall system performance such that the design is dynamic, efficient and cost-effective. In addition to creating an accurate model of the entire system, it is also important to model the real-world operating and fault conditions. For fast prototyping and performance prediction, computer-based simulation has been widely adopted in the engineering development process. Modeling such complex systems while including switching power electronic converters requires a powerful and robust simulation tool. Furthermore, a rapid solver is critical to allow for developing multiple iterative enhancements based on insight gained through system simulation studies.

PLECS is a simulation platform developed for power electronic engineers that allows for very efficient and robust modeling of such systems with multi-physical domains and associated controls. This application note presents a DFIG wind turbine system that is designed in detail using PLECS, where components from its different physical domain libraries, including electrical, magnetic, thermal and mechanical, as well as signal processing and control systems, are coupled together and the effects of the multi-domain interactions are investigated.

2 System Overview

2.1 Power in the wind

Wind turbines are capable of converting only a portion of the available wind power into mechanical power due to mechanical design considerations of the system. This mechanical power is expressed as:

$$Pmech = \frac{1}{2}\rho A C_p v^3, \tag{1}$$

where ρ is the air density, A is the area swept by the turbine blades, C_p is the performance coefficient of the turbine, and v is the wind velocity. For steady-state calculations of the mechanical power, the typical $C_p(\lambda, \beta)$ curve can be used [1] , as shown in Fig. 1.

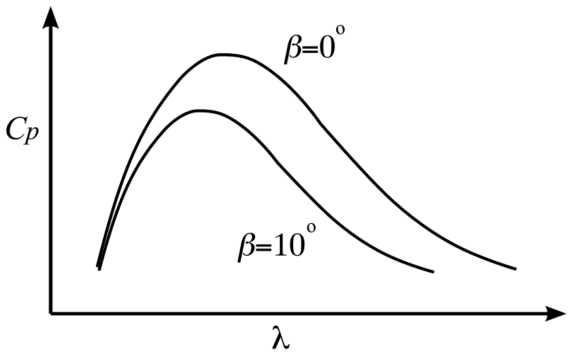

Fig. 1: Typical performance coefficient vs. tip speed ratio curve.

In the curve, β represents the blade pitch angle and λ is the tip speed ratio, given by:

$$\lambda = \frac{\Omega R}{v}, \tag{2}$$

where Ω is the mechanical rotational speed of the turbine and R is the turbine radius. It can be observed that a certain turbine rotational speed must be maintained in order to achieve the maximum mechanical power input under a given wind speed and blades pitch angle. In normal operation the pitch angle remains constant, while in special cases such as under strong winds, the pitch control is activated to shed the excess wind power and protect the wind turbine from damage.

2.2 Electromagnetic system

The electrical part of the DFIG wind turbine consists of a wound-rotor type induction machine. The machine's stator terminals are directly connected to the medium-voltage grid via a three-winding transformer, while the rotor is excited by one end of the power electronic converter, consisting of two AC-DC converters in a back-to-back configuration with a common DC-link bus. The grid-side of the converter feeds the rotor power into the grid via the transformer's tertiary winding. The system overview is shown in Fig. 2.

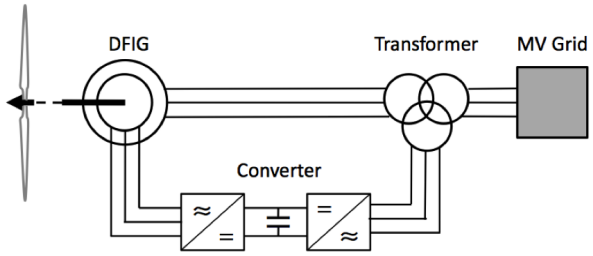

Fig. 2: System overview of the wind turbine with DFIG.

Under a limited variable-speed range (e.g. $\pm 30\%$) the converter only needs to handle a percentage $(20 - 30\%)$ of the total power [2], which in steady-state is given by:

$$P_r = \frac{s}{1-s} P_{mech}, \tag{3}$$

The power flow on the stator is given by:

$$P_s = \frac{P_{mech}}{1-s}, \tag{4}$$

In both of the above equations, s is the slip of the machine, and is defined by:

$$s = \frac{\omega_1 - \omega}{\omega_1}, \tag{5}$$

where ω_1 is the stator electrical rotational frequency, which is synchronous with the grid, and ω is the electrical rotational speed of the machine. The DFIG configuration is significantly more cost effective and less lossy as compared to a configuration using a permanent magnet generator (PMSM), which is the other common option and where the converter uses the full power range.

2.3 Cooling system

Power is dissipated during the wind turbine's operation, in part due to the conduction and switching losses of the semiconductor devices (IGBTs and diodes) in the converter. The power losses not only reduce the available electrical power that can be fed into the grid but also lead to high junction temperatures, which may destroy the semiconductor devices. Therefore, a proper cooling system should be used with the converter system such that as much heat-conduction will be transferred away from the semiconductors as is possible.

2.4 Mechanical system

The rotational components of the wind turbine couple the mechanical and electrical systems. The three blades transfer the wind torque to the hub shaft, which is connected to a gearbox. Using a specific gear ratio the gearbox boosts the rotational speed of the hub shaft onto the shaft of the induction machine's rotor. The coupling between the components shows elastic and damping effects due to the material characteristics, and friction occurs on the bearings, which also leads to power losses.

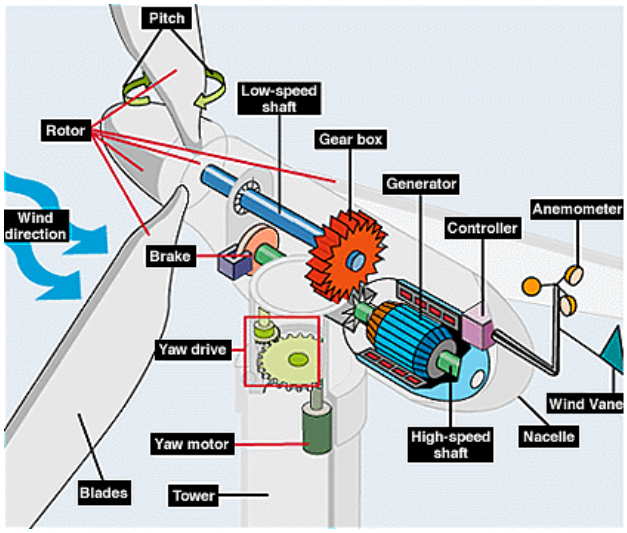

Fig. 3: Mechanical system of a wind turbine.

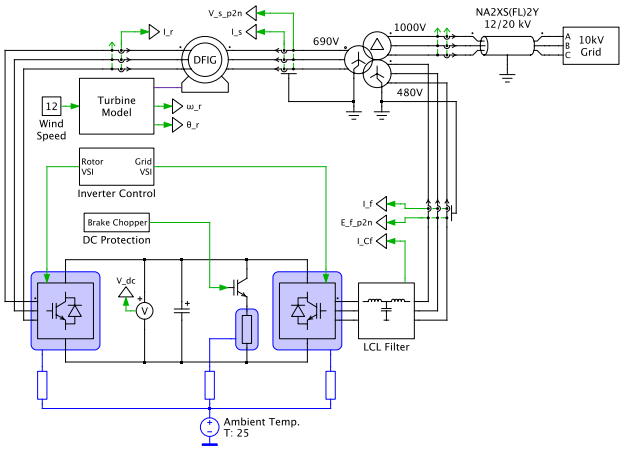

Fig. 4: Schematic of the DFIG wind turbine model in PLECS.

3 Modeling in PLECS

A 2 MW DFIG wind turbine model has been designed in PLECS and a top-level diagram is shown in Fig. 4. The components of the system are from the libraries for the different physical domains, including electrical, magnetic, mechanical, as well as signal processing and control systems.

3.1 Electrical domain

The wound-rotor induction machine, power electronic converter and LCL filter, as well as the long distance transmission line and medium-voltage (MV) grid are all modeled in the electrical domain:

- **Induction machine**: The wound-rotor induction machine model (the "Induction Machine (Slip Ring)" library component) is based on a stationary reference frame (Clarke transformation). A proper implementation of the Clarke transformation facilitates the connection of external inductances in series with the stator windings, which in this case are the leakage inductances of the transformer. External inductors cannot be connected to the rotor windings though, due to the fact that the electrical interfaces there are modeled as controlled current sources.

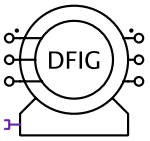

Fig. 5: The PLECS induction machine component.

- **Power converter**: The back-to-back converter topology is selected for control of the rotor power, where two three-leg, two-level IGBT bridges are connected together via a DC-link capacitor. For protection reasons a chopper IGBT and break resistor is connected onto the DC-link to clamp the capacitor voltage to a safe level. The switch will be turned on to discharge the DC-link in the case of overvoltage conditions, and turned off when the voltage falls back to the nominal value. The rotor-side inverter is directly connected to the induction machine's rotor, while the grid-side inverter is connected through an LCL filter to the tertiary winding of the transformer. The IGBTs of the inverters are modeled as ideal switches to guarantee a fast simulation at system level.

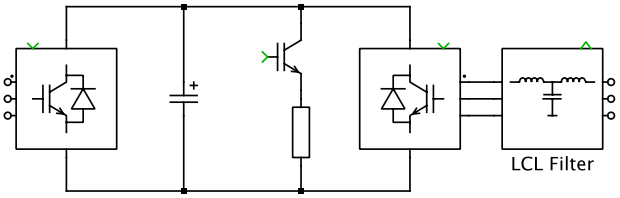

Fig. 6: Back-to-back converter model.

- **Filter**: The LCL-type filter is used to smooth the current ripple caused by the PWM modulation of the grid-side inverter. According to the electric grid code for renewable energy generation, a certain THD standard needs to be fulfilled when selecting the inductance and capacitance values. In comparison to the inductor-only filter, the LCL filter is able to suppress the harmonics with much smaller inductance values, and the reduced weight and volume therefore leads to a higher power density. Two resonant frequencies are introduced into the system due to the capacitor, however, which may give rise to stability issues [3].

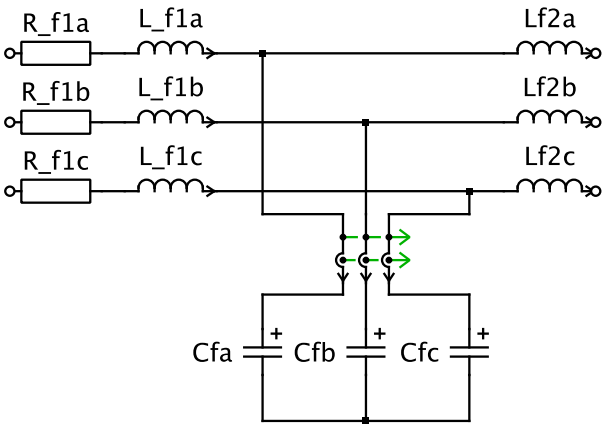

Fig. 7: LCL filter model.

- **Transmission line**: The wind capacity is strongly influenced by an area's geography. Wind turbines are often placed far from the high voltage-to-medium voltage (HV/MV) substation, so the transmission line (normally an underground cable in Europe) that transfers the wind power to the upper-level grid can be tens of kilometers in length. To model a cable of such a long distance, one can either connect multiple PI-sections (capacitor-inductor-capacitor) together in series, or imitate the traveling-wave behavior of the current and voltage. Both options are provided in the transmission line model found in PLECS and can be selected based on different requirements. The PI-section implementation is intuitive to the user, however, implementing an accurate cable model with it requires many sections. This create a large number of state variables and may slow down the simulation drastically. The distributed parameter line implementation based on the analytical solution of a traveling wave calculates the delay time of the current or voltage waveform as it propagates from one end of the cable to the other [4], and thus avoids the simulation speed issue related to an increase in state variables. But unlike the PI-section implementation, it models the power losses as lumped resistances, and only the case of symmetrical parameters (e.g. inductance) among the three phases can be modeled.

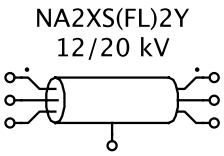

Fig. 8: The PLECS transmission line component.

- **MV grid**: The medium-voltage grid is simplified as a three-phase voltage source with a line-to-line voltage of $10\,\mathrm{kVrms}$.

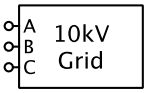

Fig. 9: Medium-voltage grid model.

3.2 Magnetic domain

The three-phase, three-winding transformer interfaces the $10\,\mathrm{kV}$ medium-voltage grid and the low-voltage terminals of the DFIG. A voltage of $690\,\mathrm{V}$

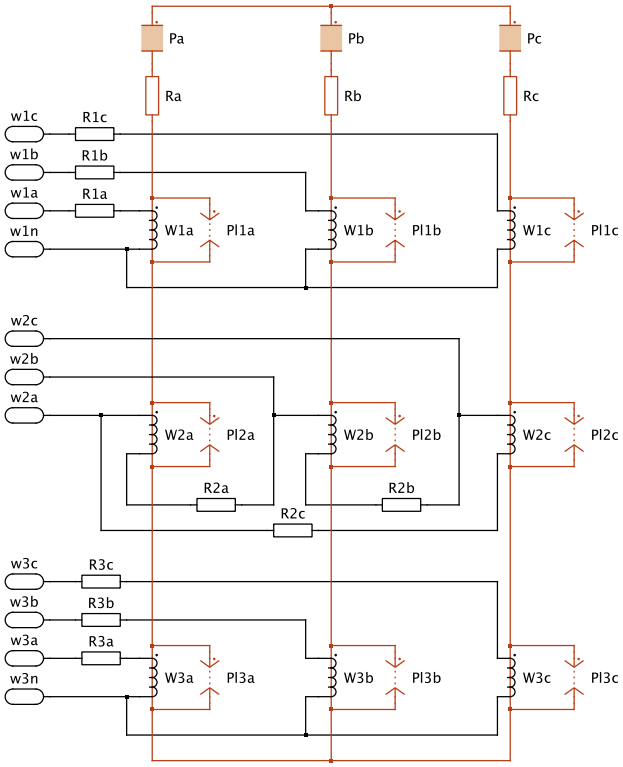

Fig. 10: Transformer model in the PLECS magnetic domain.

(line-to-line rms) is chosen for the stator-side of the DFIG, while $400\,\mathrm{V}$ is used for the rotor-side. In order to eliminate the influence of the zero-sequence component, the windings have a Δ-connection at the $10\,\mathrm{kV}$ side and a midpoint grounded Y-connection at the low-voltage side. The transformer is modeled using components from the PLECS magnetic library. Magnetic modeling in PLECS offers a powerful method for modeling such components by directly capturing a magnetic circuit using windings and lumped core parts with user-specified geometries. These core parts are represented as lumped permeances and connected with each other in PLECS to create a magnetic circuit [5]. Compared to a co-simulation with a finite element analysis (FEA) tool, where magnetic field analysis is used in the modeling of a magnetic structure, this lumped magnetic circuit method is able to integrate magnetic component models into a system level simulation without causing any substantial increase in simulation time. It also provides more details than modeling a magnetic structure as a purely electrical equivalent circuit, such as nonlinearities caused by saturation and hysteresis [6]. In addition, the separation of electrical and magnetic domains provides the user a clearer overview when approaching the actual hardware construction. In this model, the $\mathrm{YY}\Delta$ connected three-leg iron core transformer with laminated material is designed and each leg is modeled as a magnetic

permeance. Eddy current power losses are represented by magnetic resistance components, which are series-connected to the permeances. The winding components serve as the interface between the electrical and magnetic domains, and leakage fields are modeled with leakage permeances, which are connected in parallel to the windings in the magnetic domain. The complete model is shown in Fig. 10, where the linear permeance core components can be replaced by permeances with saturation or permeances with hysteresis to simulate nonlinear effects.

3.3 Thermal domain

The semiconductor power losses of the voltage source inverters play an important role in the converter design and can be investigated using PLECS' thermal domain. The PLECS ideal switch approach yields fast and robust simulations. Accurate conduction and switching loss calculations of the IGBT (and diodes) are achieved via look-up tables that are easily populated with values from data sheets.

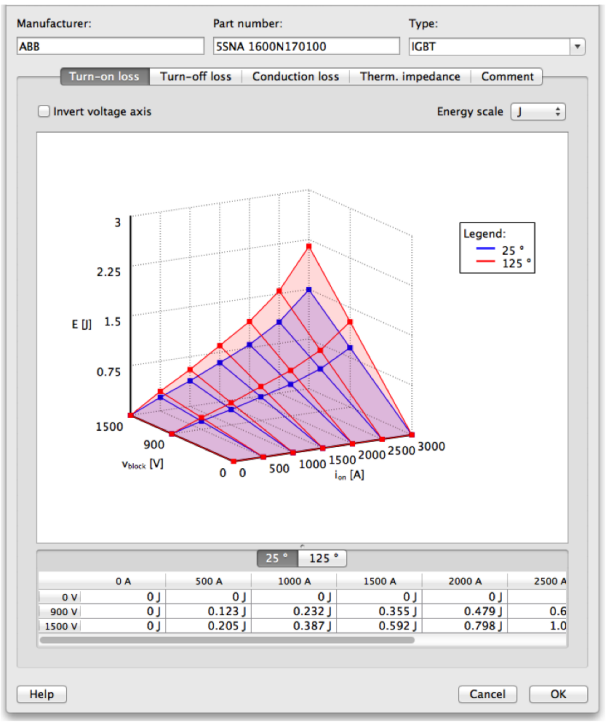

Fig. 11: The PLECS thermal look-up table interface. This shows the turn-on loss table for an IGBT.

Fig. 11 demonstrates the two dimensional look-up table for turn-on losses in PLECS, with values obtained from a data sheet [ABB's IGBT module 5SNA1600N170100]. The data sheet provides the curve of the loss energy vs. conducting current, however, for only one blocking voltage condition (1500 V). The loss values for other blocking voltages are linearly extrapolated from 0 V, which has been verified as a acceptable approximation in practice. The dependence of temperature in determining power losses can be established, and the thermal energy transfer characteristics from the junction to the case can be specified.

The PLECS heat sink component absorbs the power losses produced by the components that it contains. It feeds these losses to the cooling system, which is simply modeled in this case as a thermal resistance. The ambient temperature is modeled as a constant temperature sink. During the simulation, the junction temperature of the IGBTs can be monitored to ensure the cooling system is properly sized. Major and minor temperature cycles of the semiconductor dies can be used for life and reliability analyses.

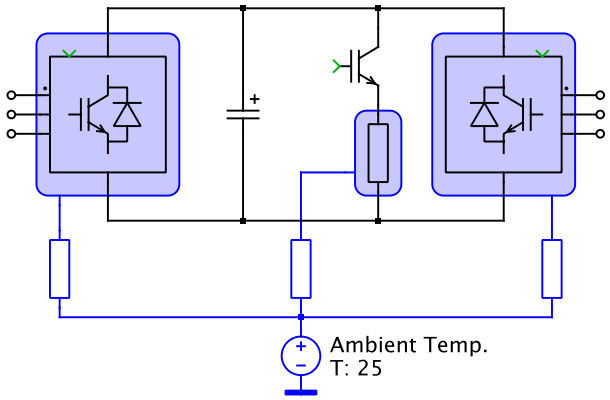

Fig. 12: Cooling system modeled in the thermal domain.

3.4 Mechanical domain

The variations of the aerodynamic torque on the blades and, consequently, electrical torque on the induction machine's rotor are propagated to the drivetrain of the wind turbine. The resulting fluctuations of the rotational speeds can lead to disturbances in the electrical domain, which depend substantially on the torsional characteristics of the drivetrain to dampen out the oscillations. This model uses a wind source to perturb the mechanical system in order to investigate the effects of such system resonances. The three blades transfer the wind torque to the hub shaft, which is connected to a gearbox. Using a specific gear ratio, the gearbox increases the rotational speed of the hub shaft onto the induction machine's rotor shaft. Friction occurs on the bearings, leading to additional power losses. The mechanical portion of this model consists of a number of lumped inertias [7], which are elastically coupled with each other, as shown in Fig. 13 and Fig. 14.

The inertias of the three blades are shown as

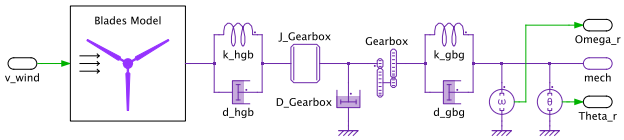

Fig. 13: Complete drivetrain modeled in the PLECS mechanical domain.

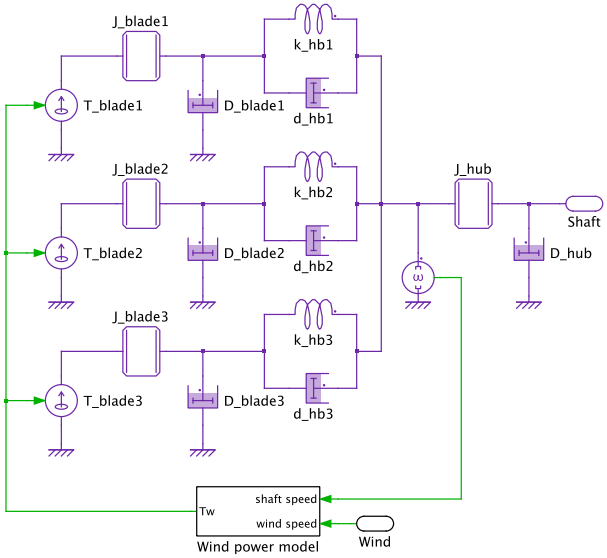

Fig. 14: Propeller drivetrain model.

J_blade1, J_blade2, and J_blade3, J_hub is the hub inertia, J_Gearbox is the gearbox inertia, and the inertia of the induction machine's rotor is included under the machine component mask. The spring constants k_hb1, k_hb2, k_hb3, k_hgb, and k_gbg model the elasticity between adjacent masses and d_hb1, d_hb2, d_hb3, d_hgb, and d_gbg represent the mutual damping. J_blade1, J_blade2, and J_blade3, J_hub, and J_Gearbox model the friction in the system, which produces torque losses on individual masses.

A wind torque input depending on wind speed and propeller rotational speed is provided. As mentioned previously the typical $C_p(\lambda, \beta)$ curve can be adopted for modeling this, and can be transformed to a surface of wind torque vs. wind speed and turbine rotational speed as shown in Fig. 15.

3.5 Control design

A proportional-integral (PI) controller with active damping and anti-windup is utilized for the control of the machine-side and grid-side inverters, as described in [2]. The main task of the machine-side inverter is to regulate the DFIG torque and thus the rotational speed of the rotor, as well as the DFIG reactive power that is injected into the grid via the induction machine's stator windings. The speed control scheme comprises an inner fast current loop

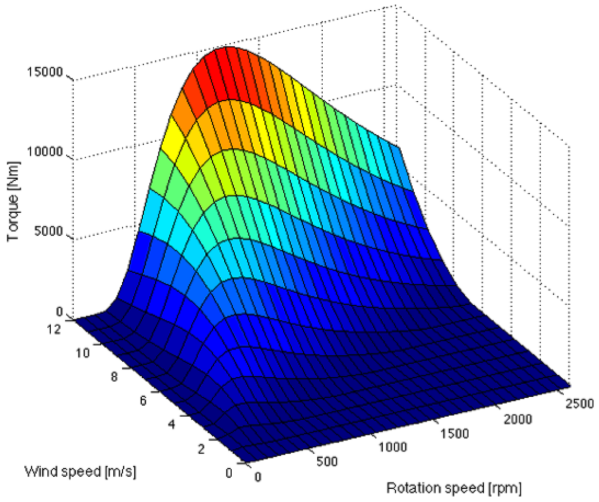

Fig. 15: Wind torque vs. wind speed and turbine rotational speed surface.

that regulates the rotor current and an outer slow speed loop, which provides the reference signal for q-axis current control. A similar structure is utilized for reactive power control.

The current control is implemented in a flux-oriented manner, where the rotor current is decomposed into the d- and q-axis in the rotational frame, which are DC values during steady state. For parameter selection the state-space model of the induction machine is derived in a form of complex vectors, where the physical variables have been transformed to the stator-side using the turns ratio:

$$v_s = R_s i_s + \frac{d\Psi_s}{dt} + j\omega_1 \Psi_s \tag{6}$$

$$v_R = R_R i_R + \frac{d\Psi_R}{dt} + j\omega_2 \Psi_R, \tag{7}$$

where

$$\Psi_s = L_M(i_s + i_R) \tag{8}$$

$$\Psi_R = (L_M + L_\sigma) i_R + L_M i_s \tag{9}$$

$$\omega_2 = \omega_1 - \omega \tag{10}$$

Note that the stator leakage inductance has been eliminated in the equations above, due to the fact that the stator flux is selected as the reference vector. Graphically the state-space model can be expressed as a circuit schematic for the d- and q-axis, respectively, as shown in Fig. 16.

By substituting the equations for the stator voltage and flux linkage into the one for the rotor voltage, we find that:

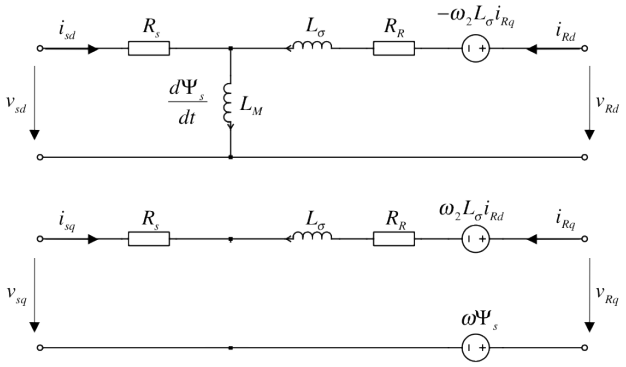

Fig. 16: State-space model of the induction machine in the rotational frame.

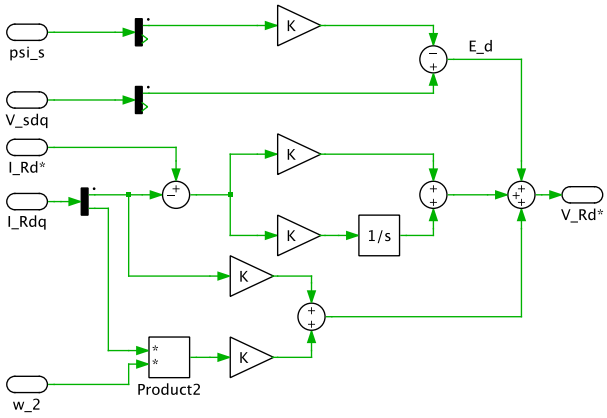

Fig. 17: D-axis current controller of the machine-side inverter.

$$v_R = (R_R + R_s + j\omega_2 L_\sigma) i_R + L_\sigma \frac{di_R}{dt} + E, \quad (11)$$

where the back EMF, E, is equal to:

$$E = v_s - (\frac{R_s}{L_M} + j\omega\Psi_s) \quad (12)$$

Rewriting the equations in the d-q axes separately yields:

$$v_{Rd} = (R_R + R_s) i_{Rd} - \omega_2 L_\sigma i_{Rq} + L_\sigma \frac{di_{Rd}}{dt} + v_{sd} - \frac{R_s}{L_M}\Psi_s \quad (13)$$

$$v_{Rq} = (R_R + R_s) i_{Rq} + \omega_2 L_\sigma i_{Rd} + L_\sigma \frac{di_{Rq}}{dt} + v_{sq} - \omega\Psi_s \quad (14)$$

The two equations above express the state-space model of the rotor current i_R with the rotor voltage v_R as the input variable. Variation of the back EMF may lead to tracking error, and like the cross coupling term from the other orthogonal axis, can be regarded as a disturbance. Such disturbances can be suppressed effectively via feedforward control. The resulting structure of the current controller is shown in Fig. 17 and Fig. 18. The output of the current controller will be given to the space vector pulse-width modulator (SVPWM) to generate the PWM signals for the three-phase terminal of the IGBT bridge.

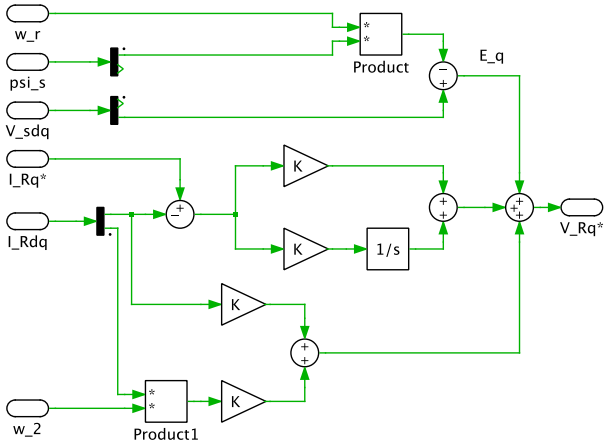

Fig. 18: Q-axis current controller of the machine-side inverter.

The stator flux linkage Ψ_s is present in the feedforward term of the back EMF, however this is not easily measured in the hardware implementation. Therefore an estimation approach using the stator current and voltage as input variables has been adopted instead [8]. Based on the implemented state-space model, the proportional and integral gains of the PI controller are selected as:

$$K_p = \alpha_c L_\sigma \quad (15)$$

$$K_i = \alpha_c (R_R + R_s + R_a), \quad (16)$$

where α_c is the desired bandwidth of the closed-loop system. It can be related to the rise time of a step response as:

$$\alpha_c = \frac{ln(9)}{t_{rise}} \quad (17)$$

Also, a virtual resistance R_a has been introduced to make sure that the disturbance (e.g. the estimation error of the back EMF) will be dampened with the

same time constant as the forward control scheme, which is also known as "active damping". R_a is defined as:

$$R_a = \alpha_c L_\sigma - R_R - R_s \tag{18}$$

The reference signal for the q-axis current is provided by the speed controller, whose design is based on the simplified mechanical model of the wind turbine:

$$\frac{J_{total}}{n_p}\frac{d\omega}{dt} = T_e - T_{wind}, \tag{19}$$

where J_{total} is the total sum of the inertia of all the masses transformed to the high-speed side of the gearbox, n_p is the number of pole pairs, T_e is the electrical torque applied on the induction machine's rotor, and T_{wind} is the wind torque transformed to the high-speed side of the gearbox. An "active damping" term is also introduced here to improve the damping of the disturbances. To avoid overshoot problems due to the clamping of the regulator outputs, an anti-windup method is used.

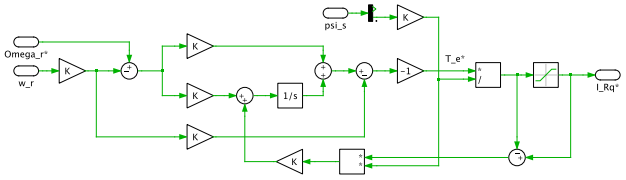

Fig. 19: Speed controller of the machine-side inverter.

At the output of the speed controller, the reference torque is converted to a current signal using:

$$i^*_{Rq} = \frac{2T_e}{3n_p\Psi_s} \tag{20}$$

In a real wind turbine system, the turbine power controller often uses a maximum power point tracking (MPPT) scheme to provide the reference signal for the speed controller. In this case however, an MPPT scheme is not modeled considering the relatively short time range of the simulation and a constant value is instead given as the speed reference.

The reference signal of the d-axis current controller is given by the reactive power controller. According to the regulations of German transmission system operators [9], the wind generator should be able to provide voltage support in terms of inductive or capacitive reactive power injection during fault conditions. The instantaneous apparent power which is absorbed by the induction machine's stator terminals can be expressed in form of a complex vector:

$$S_s = 3v_s i^*_s = 3(R_s i_s + \frac{d\Psi_s}{dt} + j\omega_1)i^*_s \tag{21}$$

Under the assumption that the stator flux linkages change only slightly, the reactive power can be expressed in the d-q frame with the derivative term neglected:

$$Q_s = 3\omega_1(\Psi_{sd}i_{sd} + \Psi_{sq}i_{sq}) \tag{22}$$

In a stator flux oriented system the q-axis component of the stator flux is zero, so the equation above becomes:

$$Q_s = 3\omega_1\Psi_s i_{sd} = 3\omega_1(\frac{\Psi_s}{L_M} - i_{Rd}) \tag{23}$$

This is rewritten as:

$$i^*_{Rd} = \frac{\Psi_s}{L_M} - \frac{Q_s}{\omega_1} \tag{24}$$

In this way a static algebraic relationship is established between the reactive power and d-axis rotor current, and an integral controller (I controller) is applied, as shown in Fig. 20. The integral factor of the I controller is given as:

$$K_{iQ} = -\frac{\alpha_Q}{3\omega_1\Psi_s}, \tag{25}$$

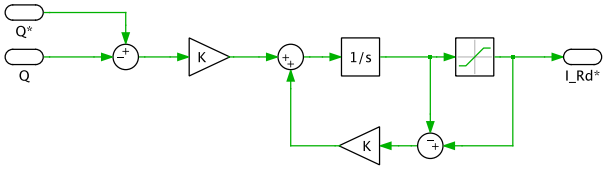

Fig. 20: Reactive power controller of the machine-side inverter.

where α_Q is the desired bandwidth. Considering the fact that the stator resistance is usually small, the stator flux Ψ_s in the equation above can be replaced by $\omega_1 V_{g,nom}$, where $V_{g,nom}$ is the nominal grid peak voltage on the stator-side of the induction machine.

The grid-side inverter maintains the DC-link voltage at a constant level. Similar to the machine-side inverter, a two-loop configuration is set up for the grid-side inverter with an outer loop for voltage control and an inner loop for current control. The current control loop is implemented in the d-q frame and is synchronized with the grid voltage, where the orientation reference is provided by a phase-locked loop (PLL).

An LCL filter is selected for the AC output terminal. Currently, this type is considered to be an attractive

solution to attenuate the switching frequency current ripple compared to the pure inductance filter due to the lower size of the magnetic components. Given the maximum ripple current I_{hfpp} (peak-to-peak) on the inverter output terminal, the inductances L_{f1a}, L_{f1b}, and L_{f1c} in Fig. 7 can be determined by:

$$L_{f1} = cos(\frac{\pi}{6})\frac{2/3V_{dc}-V_{g3}}{I_{hfpp}f_{sw}}\frac{\sqrt{3}V_{g3}}{V_{dc}}, \tag{26}$$

where V_{g3} is the nominal voltage (peak value) on the tertiary winding of the transformer. The ratio between the inductance values L_{f1} and L_{f2} can be treated as an operational variable for optimization of overall size and cost. In this model it is assumed that a value of $L_{f2} = 0.15L_{f1}$ has been chosen as a result of the optimization. According to the THD requirement for the grid operator, which is the ratio between the peak-to-peak value of the nominal grid current I_{gpp} and ripple I_{hfpp}, the capacitance value can be calculated as:

$$C_f = 1\frac{1}{L_{f2}(2\pi f_{sw}10^{\frac{k_A}{40dB}})^2}, \tag{27}$$

where the attenuation k_A is given as:

$$k_A = 20log_{10}(THD\frac{I_{gpp}}{I_{hfpp}}) \tag{28}$$

4 Model Parameters and Simulation Scheme

The electrical parameters of the doubly-fed induction machine according to [10] are listed below in Table 1, where the rotor parameters have been converted to the stator-side using the turns ratio.

Table 1: Electrical parameters of the induction machine.

Pole pairs n_p	2
Turns ratio n_s/n_r	1/2.6
Stator leakage $L_{s\sigma}$	0.12 mH
Rotor leakage $L'_{r\sigma}$	0.05 mH
Main inductance L_m	2.9 mH
Stator resistance R_s	0.022 Ω
Rotor resistance R'_r	0.0018 Ω

The transformation from the physical parameters in Table 1 above to the ones of the equivalent circuit in Fig. 16 is achieved via the following equations:

$$L_M = \gamma L_m \tag{29}$$

$$L_{sigma} = \gamma L_{s\sigma} + \gamma^2 L'_{r\sigma} \tag{30}$$

$$R_R = \gamma^2 R_r, \tag{31}$$

where

$$\gamma = (L_{s\sigma} + L_m)/L_m \tag{32}$$

As a result of the aforementioned design process for the LCL filter, the inductance value of the converter-side as well as grid-side inductors are calculated as $0.48\,\mathrm{mH}$ and $0.044\,\mathrm{mH}$, respectively, while the capacitance value is $57\ \mu\mathrm{F}$. For connection from the turbine transformer to the $10\,\mathrm{kV}$ stiff grid, the model of a $10\ \mathrm{kV}$ medium-voltage cable (type N2XSF2Y [10]) is established using the distributed parameter line component. The resistance, self-inductance and neutral capacitance per unit length are $0.206\ \Omega/\mathrm{km}$, $0.363\ \mathrm{mH/km}$ and $0.25\ \mu\mathrm{F/km}$, respectively. The mutual inductance and coupling capacitance are assumed to be one third of the self- and neutral values. The mechanical parameters of an example $2\,\mathrm{MW}$ wind turbine are provided by [10] and [7] in per unit values, and the transformation from per unit to real values has been described in [11].

Table 2: Mechanical parameters of the wind turbine.

Rotor inertia J_g	$75\ \mathrm{kgm^2}$
Gearbox inertia J_{gb}	$4.26 \times 10^5\ \mathrm{kgm^2}$
Hub inertia J_h	$6.03 \times 10^4\ \mathrm{kgm^2}$
Blade inertia J_b	$1.13 \times 10^6\ \mathrm{kgm^2}$
Rotor friction D_g	$0.81\ \mathrm{Nms/rad}$
Gearbox friction D_{gb}	$1.78 \times 10^4\ \mathrm{Nms/rad}$
Hub friction D_h	$8.11 \times 10^3\ \mathrm{Nms/rad}$
Blade friction D_b	$1.08 \times 10^3\ \mathrm{Nms/rad}$
Gearbox to rotor stiffness k_{gbg}	$4.67 \times 10^7\ \mathrm{Nms/rad}$
Hub to gearbox stiffness k_{hgb}	$1.39 \times 10^1\ \mathrm{Nms/rad}$
Blade to hub rotor stiffness k_{bh}	$1.07 \times 10^1\ \mathrm{Nms/rad}$
Gearbox to rotor damping d_{gbg}	$0.81 \times 10^3\ \mathrm{Nms/rad}$
Hub to gearbox damping d_{hgb}	$2.84 \times 10^6\ \mathrm{Nms/rad}$
Blade to hub rotor damping d_{bh}	$3.24 \times 10^6\ \mathrm{Nms/rad}$

During the simulation the following example scenarios are executed successively:

- **Initial state**: At the simulation start the generator operates at $157\ \mathrm{rad/s}$, which is synchronous to the grid frequency. Most of the generated active power is injected into the grid via

the stator winding of the induction machine, while due to the zero slip condition, virtually no power flows through the rotor except for the resistive losses. The reactive power generation is not activated yet at this stage.

- **Acceleration**: At 3 s the rotation speed of the turbine is accelerated to 175 rad/s via a step jump on the reference input of the speed controller, to achieve maximum power generation under the given wind speed of 12 m/s. As mentioned previously, the external MPPT loop utilized in a practical implementation is not present in this model. The step change of the speed reference is just a fictional one which sets up the machine for an extreme test case to prove the system's stability.

- **Grid fault**: At 12 s a three-phase short circuit fault occurs on the 10 kV medium-voltage grid, which is modeled using a controllable voltage source. Three fault options regarding the residual voltage's profile can be chosen. The first option is a 0.2 s zero voltage sag, while the other two options are described in the 2007 German Transmission Code Standards [9], as Fig. 21 shows.
  The duration of the simulation has been set to 25 s, which should be sufficient to investigate the reaction from the overall system standpoint, especially considering the mechanical part. This timeframe is however, relatively long compared to the switching frequency of the back-to-back converter (5 kHz). If the current ripple due to the switching frequency and power losses of the semiconductors are not of interest for certain applications, an averaged converter model can be used to speed up the simulation. The averaged model is established via controlled voltage and current sources, as shown in Fig. 22, and can be optionally selected from the mask.

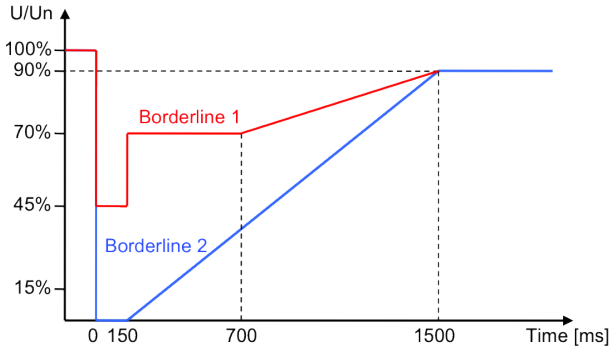

Fig. 21: Voltage profiles during the event of a grid fault.

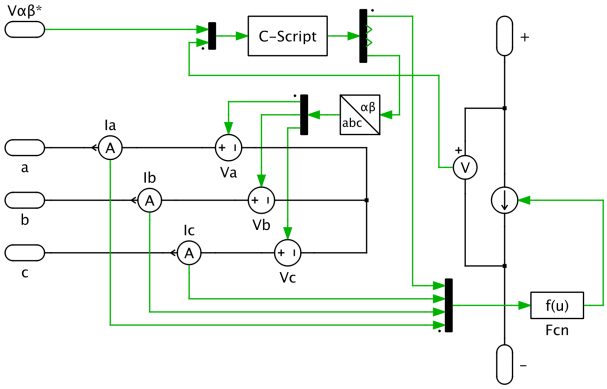

Fig. 22: Averaged model of the three-phase inverter.

5 Results and Discussion

By simulating the scenarios described above, the robustness of the design is observed and improvements can be made, namely with the control techniques. The various parameters in the system are chosen to provide desirable results during the entire operating range of the turbine. At the start of the simulation, a damped oscillation can be observed due to the elastic and lossy coupling between the mechanical parts, as shown in Fig. 23.

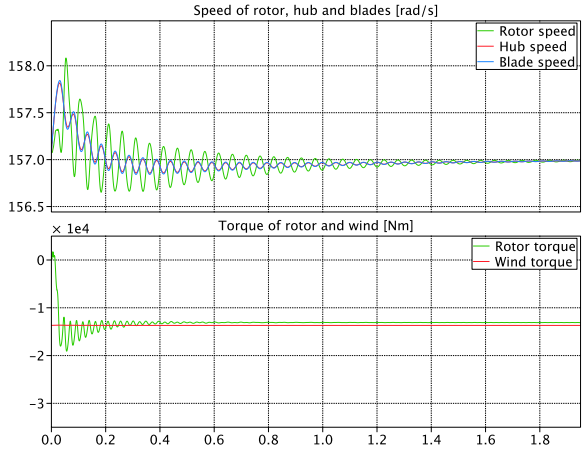

Fig. 23: Mechanical oscillation at startup of the wind turbine.

As the step change for the speed reference is applied, the speed controller generates a torque reference for the q-axis current controller of the machine-side inverter which is higher than the wind torque applied on the blades, thus the turbine accelerates. The behavior of rotational speed and torque is illustrated in Fig. 24, where the speed values of the hub and blades have been converted to the high-speed side of the gearbox (the induction machine shaft side). After approximately 7 s, the electrical torque of the induction machine and the wind torque enter a balanced state and the rota-

tional speed remains $175\ \mathrm{rad/s}$. As a result of the -11% slip rate, about 10% of the real power will now be transmitted out of the rotor winding, as shown in Fig. 25.

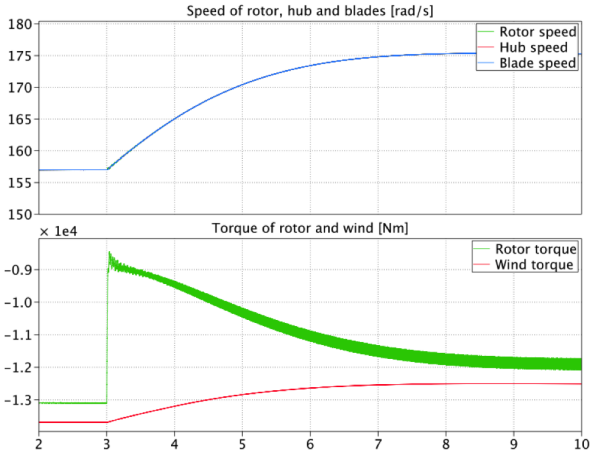

Fig. 24: Mechanical reaction during acceleration.

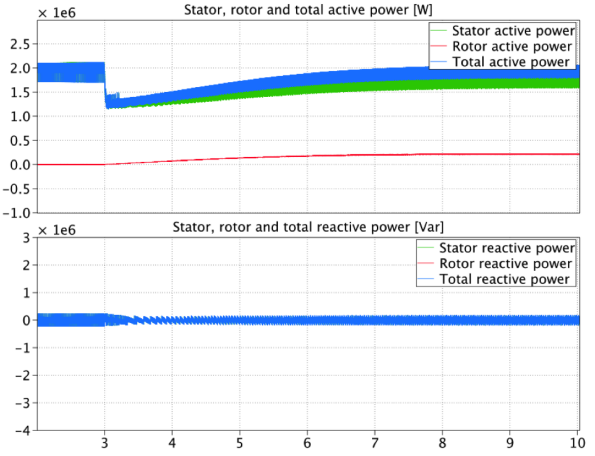

Fig. 25: Active and reactive power flow out of the stator and rotor during acceleration.

If the averaged model is chosen for the simulation, the electrical torque waveform will be ripple-free and match the mean value of the torque waveform for the model with ideal switches, as seen in Fig. 26.

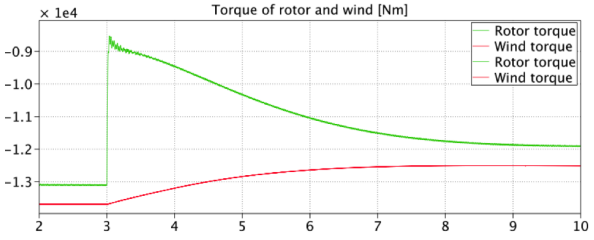

Fig. 26: Electrical torque of the induction machine in the averaged model.

To evaluate the performance of the wind turbine during a worst case grid-side fault condition, known as "low voltage ride through" (LVRT) behavior, and the *borderline 2* scenario from Fig. 21, is set up for the voltage profile during the grid short circuit. As the grid voltage falls to zero at $14\ \mathrm{s}$, the stator flux deceases to an extremely small value, where the induction machine is no longer able to generate electrical torque. When this happens, the power absorbed by the blades from the wind will be completely stored in the rotating mechanical components in the form of kinetic energy, and the turbine will accelerate. After the voltage starts to recover due to the clearing of the fault after $0.15\ \mathrm{s}$, the stator flux recovers gradually such that electrical torque can be produced again to counteract the driving torque from the wind. As a result the speed will be restored back to the reference value $175\ \mathrm{rad/s}$, as shown in Fig. 27.

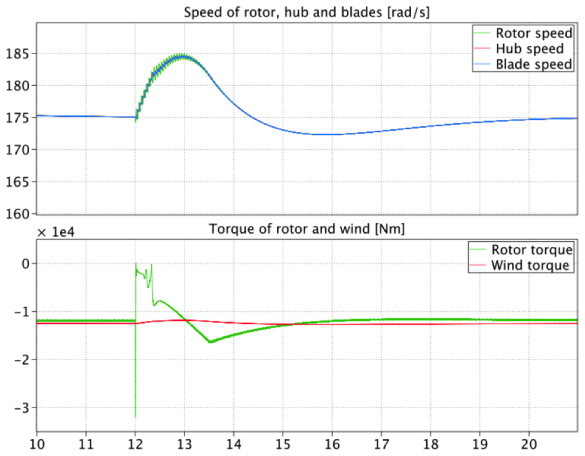

Fig. 27: Mechanical transient during the grid fault.

The electrical transient of voltage and current on the primary winding ($10\ \mathrm{kV}$ side) of the transformer, as well as the DC-link voltage of the back-to-back converter, is displayed in Fig. 28. The AC voltage on the transformer terminal does not fall to zero as the grid is stiff due to the inductance of the transmission line in between. The AC current exhibits a large peak immediately after the fault occurs, and then is maintained below a certain range because of the saturated input of the current controller. Due to the voltage drop at the transformer's tertiary winding, the grid-side inverter is also no longer able to transfer power, so the DC-link voltage is nearly uncontrolled in the first seconds after the fault. The DC-link capacitor is then charged or discharged purely by the machine-side inverter. The transient of the active power from the machine-side inverter can be analyzed using the q-axis equivalent circuit in Fig. 16.

Immediately after the fault occurs, the q-axis voltage v_{Rq} and current i_{Rq} of the rotor still remain as the same values seen during normal operation.

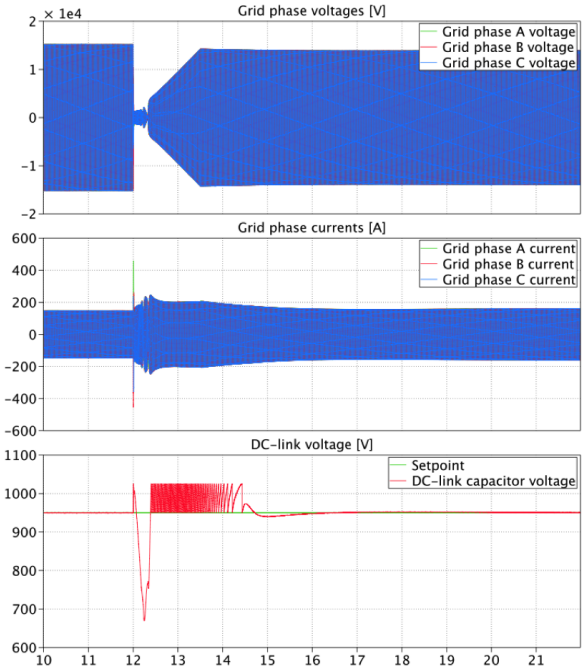

Fig. 28: Electrical transient during the grid fault.

Therefore, nearly the identical amount of active power as before the fault charges the capacitor, such that the voltage rises quickly. The voltage will not exceed 108% of the nominal voltage $(950\mathrm{V})$, however, and is clamped to a safe level due to the activation of the chopper circuit. The speed controller will then deliver a higher reference value for the q-axis current to the current controller to pull the rotational speed back to $175\ \mathrm{rad/s}$, although it is unsuccessful.

As a result, the current controller applies a q-axis voltage v_{Rq} of opposite polarity compared to before the fault, because of the nearly zero value of the back EMF $\omega\Psi_s$. Hence, the active power becomes negative for a short time, and the capacitor is discharged and the voltage falls until approximately $12.3\ \mathrm{s}$. After that, as the grid voltage recovers, the back EMF $\omega\Psi_s$ rises so v_{Rq} changes its polarity back to what it was before the fault, and the active power becomes positive, effectively re-charging the capacitor. At this moment the grid-side inverter is still not able to transfer a large amount of power, therefore the net power flowing into the capacitor is still in surplus and the voltage rises further. Because of the chopper circuit, the voltage oscillates between the limitation and the nominal value in the following several seconds, until the grid voltage totally recovers and the grid-side inverter is again able to transfer enough power.

If this fault scenario is simulated with the averaged inverter model, the result shows slight differences from that with the full switching model, because the switching period is comparable to the transient during the fault condition. This issue should be considered if the averaged model is used to accelerate the simulation speed. As shown in Fig. 29, the lighter red curve corresponds to the switched model.

The thermal information, including the junction temperature and losses for one IGBT over the course of the total simulation, is depicted in Fig. 30. Note that the switched inverter model must be enabled in order to view these waveforms.

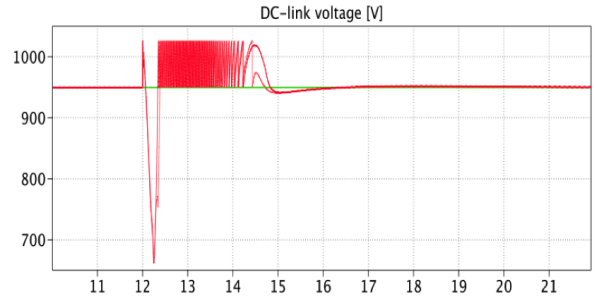

Fig. 29: Comparison of the DC-link voltage between the averaged and switched inverter model.

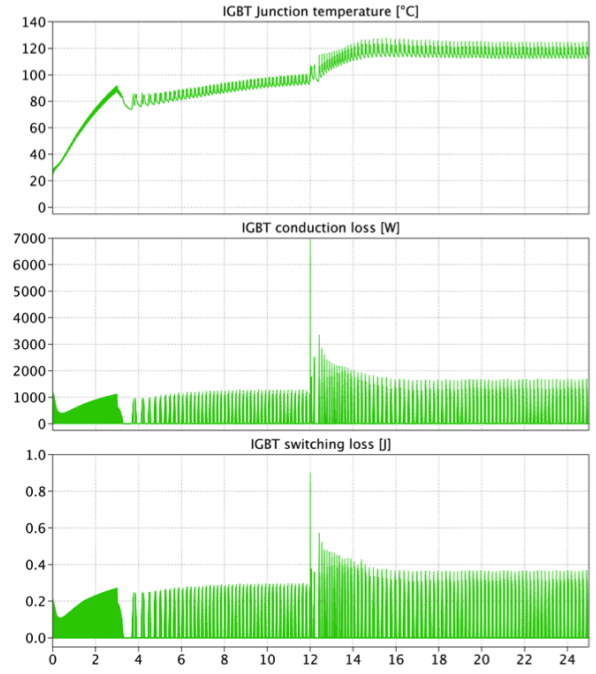

Fig. 30: Junction temperature, conduction and switching losses of one IGBT.

6 Conclusion

The modeling and simulation of a complete DFIG wind turbine model has been presented in this report. With the help of PLECS, the transient effects from multiple physical domains can be evaluated in a single system model without requiring excessive simulation times, thereby providing an effective and accurate means for investigating and addressing issues related to inter-physical domain interactions. Such fully integrated models provide power electronic designers with more insight into the system before hardware is built, leading to time and cost savings.

References

[1] J. Schönberger, "Modeling a dfig wind turbine system using plecs," in *Application Note of Plexim GmbH*.

[2] A. Petersson, *Analysis, Modeling and Control of Doubly-Fed Induction Generators for Wind Turbines*. PhD thesis, Chalmes University of Technology, Göteborg, Sweden, 2005.

[3] R. Teodorescu, M. Liserre, and P. Rodriguez, *Grid Converters for Photovoltaic and Wind Power Systems*. Aalborg: John Wiley & Sons, Ltd, 1. edition ed., 2011.

[4] H. Dommel, "Digital computer solution of electromagnetic transients in single and multiple networks," in *IEEE Transactions on Power Apparatus and Systems*, pp. Vol. PAS88, No. 4.

[5] J. van Vlerken and P. Blanken, "Lumped modeling of rotary transformers, heads and electronics for helical-scan recording," in *Control and Modeling for Power Electronics (COMPEL), IEEE 13th Workshop on*, 2012.

[6] J. Allmeling, W. Hammer, and J. Schönberger, "Transient simulation of magnetic circuits using the permeance-capacitance analogy," in *Control and Modeling for Power Electronics (COMPEL), IEEE 13th Workshop on*, 2012.

[7] S. M. Muyeen, M. H. Ali, R. Takahashi, T. Murata, J. Tamura, Y. Tomaki, A. Sakahara, and E. Sasano, "Blade-shaft torsional oscillation minimization of wind turbine generator system by using statcom/ess," in *Power Tech, 2007 IEEE Lausanne*, pp. 184–189.

[8] Analog Devices Inc, "Flux and speed estimation for induction machines," in *Application Note AN331-29*.

[9] Verband der Netzbetreiber VDN e.V. beim VDEW, "Network and system rules of the german transmission system operators," in *Transmission Code*, 2007.

[10] T. Thiringer, J. Paixao, and M. Bongiorno, "Monitoring of the ride-through ability of a 2 mw wind turbine in tvaaker, halland," in *Elforsk rapport 09:26*.

[11] A. G. G. Rodriguez, A. G. Rodriguez, and M. B. Payan, "Estimating wind turbines mechanical constants,"